Observations of cross-shore chenier dynamics in Demak, Indonesia

Tas, Silke A.J.; van Maren, Dirk S.; Reniers, Ad J.H.M.

DOI
10.3390/jmse8120972

Publication date
2020

Document Version
Final published version

Published in
Journal of Marine Science and Engineering

Journal of
Marine Science and Engineering

MDPI

Article

Observations of Cross-Shore Chenier Dynamics in Demak, Indonesia

Silke A. J. Tas [1,*], Dirk S. van Maren [1,2] and Ad J. H. M. Reniers [1]

[1] Faculty of Civil Engineering and Geosciences, Delft University of Technology, 2628 CN Delft, The Netherlands; bas.vanmaren@deltares.nl (D.S.v.M.); a.j.h.m.reniers@tudelft.nl (A.J.H.M.R.)
[2] Deltares, Boussinesqweg 1, P.O. Box 177, 2600 MH Delft, The Netherlands
* Correspondence: s.a.j.tas@tudelft.nl

Received: 03 November 2020; Accepted: 24 November 2020; Published: 30 November 2020

Abstract: Cheniers are important for stabilising mud-dominated coastlines. A chenier is a body of wave-reworked, coarse-grained sediment consisting of sand and shells overlying a muddy substrate. In this paper we present and analyse a week of field observations of the dynamics of a single chenier along the coast of Demak, Indonesia. Despite relatively calm hydrodynamics during the one-week observational period, the chenier migrated surprisingly fast in the landward direction. The role of the tide and waves on the cross-shore chenier dynamics is explored using velocity moments as a proxy for the sediment transport. This approach shows that both tide and waves are capable of transporting the sediment of the chenier system. During calm conditions (representative for the south-east monsoon season), the tides generate a landward-directed sediment transport when the chenier crest is high relative to mean sea level. Waves only generate substantial sediment transport (direct, via skewness, and indirect, via stirring) when the chenier is submerged during periods with higher waves. The cross-shore chenier dynamics are very sensitive to the timing of tide and waves: most transport takes place when high water levels coincide with (relatively) high waves.

Keywords: cheniers; field measurements; sediment transport; mangroves; muddy coast; Indonesia

1. Introduction

A chenier is a beach ridge, resting on silty or clayey deposits, which becomes isolated from the shore by a band of tidal mudflats [1,2]. Cheniers play an important role in stabilising the coast (for example, along the Amazon-Orinoco coast, where large mud banks migrate alongshore, cheniers mitigate erosion in inter-mudbank areas [3]). Cheniers can be part of an inactive delta plain (the so-called chenier plain, a multi-membered, progradational ridge/interridge mudflat sequence [2]) or manifest itself as active barriers. Chenier plains are associated with prograding littoral environments [1] or deltas [2] with a sufficient supply of fine sediments of which the relative importance varies in time [1,2]; winnowing of the fine sediment deposits gives rise to the sandy barriers. Chenier plain shores are generally characterised by low to moderate wave conditions, tides may range from micro-tidal to macro-tidal and periods of wave dominance alternate with periods of high sediment supply [1]. Nardin and Fagherazzi [4] demonstrate that chenier plains may also develop in areas with persistent high waves and without alternating periods as long as a specific balance between sediment availability and wave action exists. Chenier plain formation along actively prograding river mouths has indeed been observed along e.g., the Red River Delta, where formation of barriers is triggered by cyclic growth of the delta front under constant river supply [5]. The most extensive and most studied chenier plains are those in Louisiana (e.g., [6,7]) and along the Suriname–Guyana coastline [2,3]. Less well investigated examples include the chenier plains in China [8] and West Africa [9,10].

A poorly documented example of an active chenier system can be found along the coastline of Demak, a region along the north coast of Central Java in Indonesia. Cheniers are observed along stretches of the rapidly eroding mangrove-mud coast. Their formation may therefore result of sand winnowing from the muddy substrate, analogous to classical chenier plain formation. However, a chenier plain cannot be seen in the landscape. This could mean that the cheniers have only recently formed, possibly connected to the trend of coastal erosion starting in the early 2000s. Another explanation may be that older cheniers have disappeared due to sand mining, since sand is a commodity in a mud-dominated coast. While cheniers are traditionally observed in the proximity of large rivers (such as the Mississippi River for the cheniers along the coastline of Louisiana, or the Amazon River for the cheniers along the Suriname–Guyana coastline), the Demak coastline does not feature rivers of such size. The Wulan River at the northern border of Demak only has a fraction of the discharge of these large rivers, which suggests that the observed cheniers are not directly related to river supply. Although their origin is unknown, their presence is pivotal for the protection of the eroding coastline: van Bijsterveldt [11,12] shows that 92% of mangrove cover in Demak in 2014 was situated east, south-east or south of the nearest chenier, which means the mangroves are sheltered from the north-west (N.W.) monsoon wind and resulting waves. This confirms that mangroves (stabilising the coastline) mainly grow in areas sheltered by cheniers. As such, knowledge of their formation, dynamics and fate is crucial.

Demak borders the Java Sea, a shallow and sheltered basin, see Figure 1. The region features a tropical monsoon climate, bordering on a tropical rain forest climate [13]. During the wet monsoon season, usually November to April, the dominant wind direction is north-west, and reverses to south-east during the dry season [14].

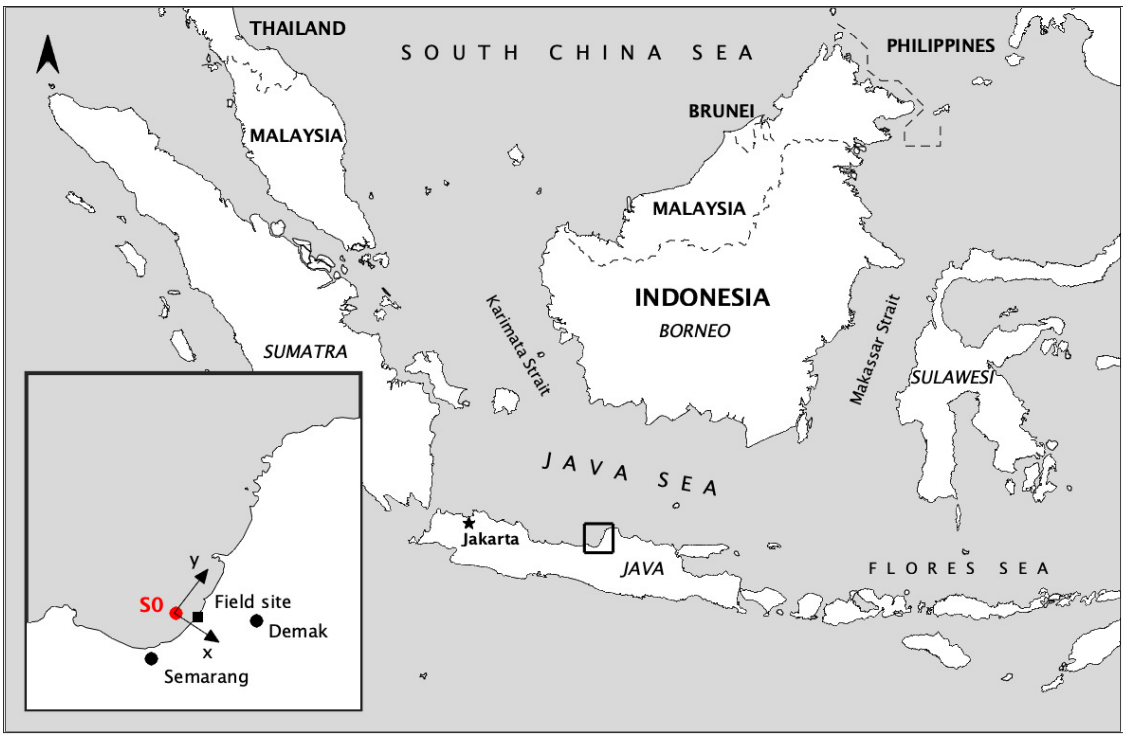

Figure 1. Map of the Java Sea. The box indicates the location of the inset map, showing the coastline of Demak on the north coast of Central Java, where the field study was conducted. The red dot on the inset map shows the position of S0, a WaveDroid measuring the offshore wave conditions.

Old Dutch colonial maps indicate that the coastal area of Demak used to be completely covered by mangroves [15]. By the turn of the 21st century, almost all mangrove cover had been replaced by fish ponds, and the area had also started suffering from land subsidence due to groundwater extraction,

natural consolidation and added load of constructions [16]. By this time, large-scale coastal erosion had started, leading to coastal retreat of more than a kilometre in some locations along the coastline of Demak by 2010. Satellite images show the appearance of cheniers in the same period. Whether they are a new phenomenon, or whether they have always been present in this system is unknown. However, there seems to be a relation between the presence of cheniers and mangrove cover [11,12]. The Google Earth image [17] in Figure 2 confirms this, showing more mangroves along chenier-sheltered sections of the coastline and erosion of exposed areas. However, the cheniers are very dynamic, so their impact on longer time scales remains unknown.

Figure 2. Google Earth image [17] taken on 4 September 2015 shows two cheniers off the coastline of Demak. Behind those cheniers, some small patches of mangrove forest are visible. North of the cheniers, where the coastline is unprotected, barely any mangrove tree persists.

Closer examination of Google Earth satellite images [17] over time reveals a relation between chenier dynamics and the monsoon period (Figure 3). During the calm and dry south-east (S.E.) monsoon season, the chenier migrates in an onshore direction, as seen in Figure 3b,c. There are no satellite images during the wet N.W. monsoon season, but the first image after the wet season reveals that the chenier has migrated in the offshore direction compared to the location before the start of the wet season (Figure 3a,d). This suggests that calm conditions induce landward migration of the chenier, while storm conditions result in a seaward migration of the chenier.

Observations (this paper) of chenier dynamics along the north coast of Central Java reveal that they are extremely dynamic and rapidly migrating in the cross-shore direction. The relative role of tides, waves and sediment supply in their dynamics is up to now insufficiently understood. Our aim is therefore to identify the physical processes that drive the dynamics of an existing chenier in the cross-shore direction. To that end we carried out an extensive field experiment capturing the hydrodynamics and morphology of one chenier over a period of six weeks. In this paper, we focus on the last week of observations, a period during which the chenier became very dynamic.

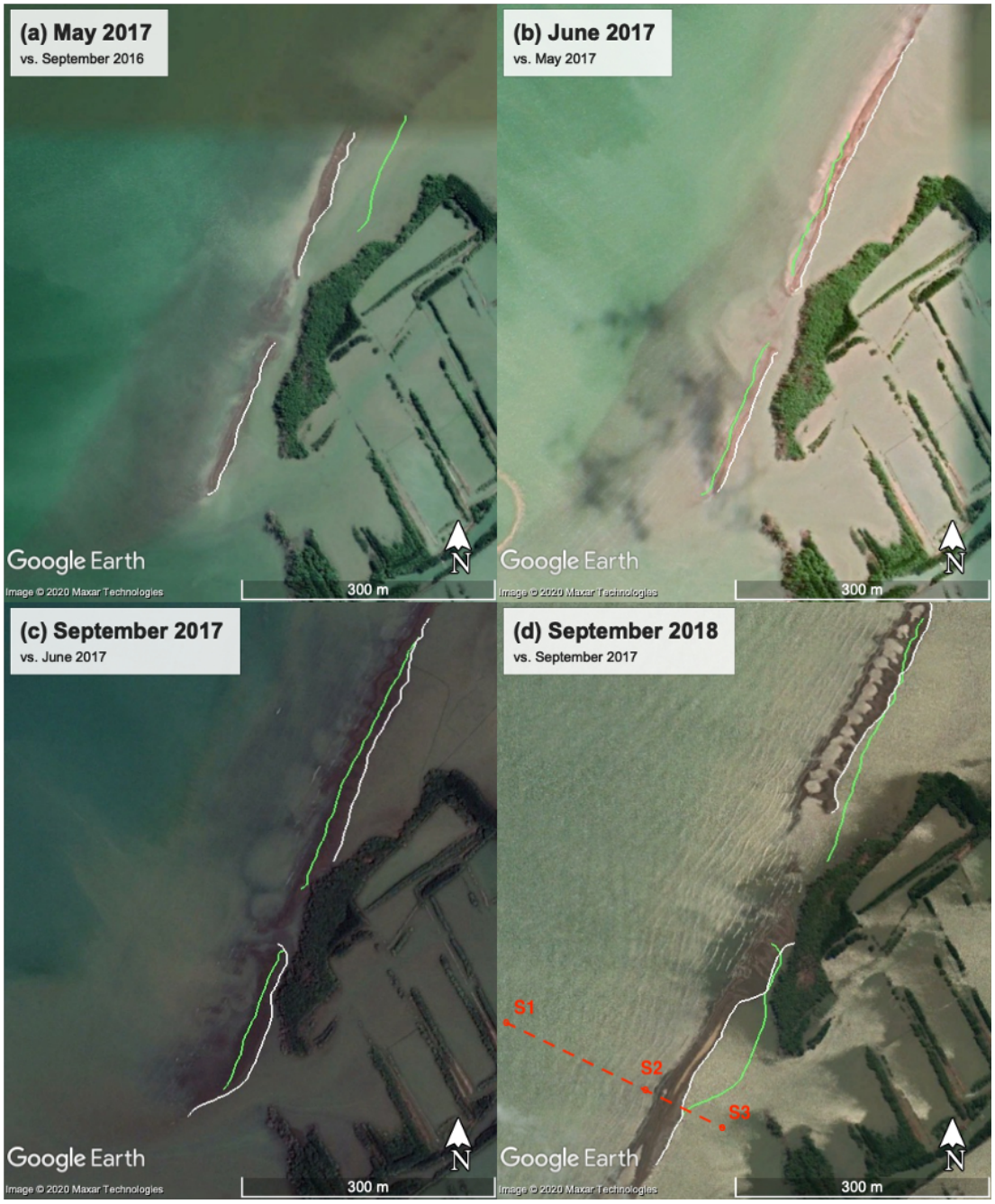

Figure 3. Google Earth images [17] illustrating that the chenier migrates landward during the calm and dry south-east (S.E.) monsoon season, and seaward over the wet north-west (N.W.) monsoon season. The white line follows the landward edge of the chenier crest at the time the image was taken, while the green line shows the location of the chenier at the time of the previous image. The red dashed line in (**d**) is the location of our observation transect in Figure 4, with S1–S3 depicting the location of instruments.

The structure of this paper is as follows. The methodology is introduced in Section 2. In Section 3 we present the field observations (Section 3.1) and analyse the mechanisms driving the cross-shore chenier dynamics, using velocity moments as a proxy for the sediment transport (Section 3.2) and Section 4 discusses the influence of the hydrodynamic conditions, the importance of the sea breeze and draws an analogue with breaker bars. The conclusions are summarised in Section 5.

2. Methods

In order to investigate the cross-shore chenier dynamics in more detail, a field study was conducted at one chenier in front of the coastal village of Timbulsloko between 25 October and 10 December 2018. The chenier is only connected to the shore at its northern extremity, where it borders a mangrove patch (the lower chenier in Figure 3). The chenier creates a bay between itself and the (severely) eroded coast. This measurement period was chosen such that it would cover the end of the (calm) S.E. monsoon season and the start of the N.W. monsoon season, with higher waves. Unfortunately, the N.W. monsoon season started later than usual, so throughout the entire field campaign, the S.E. monsoon conditions persisted. Therefore, the wave height remained low, except during afternoons when a sea breeze generated local wind waves.

Several high-resolution topographic surveys were conducted using Trimble 5700 DGPS (Differential Global Positioning System) receivers, one serving as fixed base station and the other a mobile sensor to measure the coordinates and elevation of points on the chenier. Due to problems with the base station, the absolute height of each measured profile is unknown. However, the relative height of each profile with respect to each other could be determined using data of erosion pins at the emerged part of the profile. Profiles were collected between 8 November and 8 December 2018. Additional bathymetric profiles were collected using a rod and a handheld GPS. These data were further supplemented with detailed measurements of bed level changes using erosion pins at 8 points along the transect.

Water level information was collected using three OSSI-010-003C-01 Wave Loggers, at S1, S2 and S3 (see Figure 3d), sampling at a frequency of 10 Hz. The pressure signal of the sensors was used to calculate wave spectra over intervals of 30 min, with a frequency resolution of 0.01 Hz. The sensors were placed 15 cm above the bed and the sensors at S2 and S3 emerged partly through the tidal cycle. Offshore wave data were collected using a WaveDroid® directional wave buoy, which was deployed at a water depth of 12 m, 5.5 km offshore of the chenier (location S0, see Figure 1). Current velocities were obtained using an Acoustic Doppler Velocimeter (ADV), deployed at the seaside of the chenier at S1 (see Figure 3d), measuring at a frequency of 4 Hz. The measuring volume was situated 30 cm above the bed, and the sensor emerged partly through the tidal cycle.

Sediment transport was not directly measured, but can be approximated using the flow velocity, assuming the sediment is mainly transported by bed load [18–21]. The time-averaged cross-shore sediment flux S is assumed to be proportional to the third power of the flow velocity [19], see Equation (1):

$$\overline{S} \sim \overline{u^3} \tag{1}$$

where u is the instantaneous velocity and the overbar denotes time-averaged (over a period of 30 min). Next, the velocity is decomposed into three components, $\overline{u}$ the time-averaged velocity, $\widetilde{u}$ the velocity due to the short wave motion and u_{ig} the velocity due to the infragravity waves. The frequency cut-off for the infragravity waves is set at 0.05 Hz, as longer swell and wind waves are not expected in the shallow and sheltered Java Sea. This gives:

$$\begin{aligned} \overline{S} &\sim \overline{\left(\overline{u} + \widetilde{u} + u_{ig}\right)^3} \\ &\sim \overline{\overline{u}^3 + \widetilde{u}^3 + {u_{ig}}^3 + 3\overline{u}^2\widetilde{u} + 3\overline{u}^2 u_{ig} + 3\overline{u}\widetilde{u}^2 + 3\overline{u}{u_{ig}}^2 + 3\widetilde{u}^2 u_{ig} + 3\widetilde{u}{u_{ig}}^2 + 6\overline{u}\widetilde{u}u_{ig}} \end{aligned} \tag{2}$$

Solving the third power in this equation splits the right hand side into 10 velocity moments, following Bowen [18]. By time-averaging the individual moments, some are reduced to zero, leaving four individual moments given by:

1. $\overline{u}^3$ representing the sediment transport driven by the mean current,
2. $\overline{\widetilde{u}^3}$ associated with the skewness of the short waves,

3. $3\overline{\overline{u}\widetilde{u}^2}$ due to the stirring by the short waves and subsequent transport by the mean current, and
4. $3\overline{u_{ig}\widetilde{u}^2}$ representing the transport by long waves.

The above method can be applied directly to the measured velocities at S1. However, the estimation of wave-related velocity moments from the pressure recordings at location S2 (where velocity was not measured) requires an extra step through which the instantaneous pressure is translated into horizontal velocities. Here we follow the approach of de Wit et al. [22] using linear wave theory and assuming that the wave reflection is minimal. This approach is explained in more detail in Appendix A. Comparing the velocity moments obtained from the measured velocities by the ADV with the co-located pressure recordings at location S1 shows good agreement (on 2 December, the median root mean square error (RMSE) is 16% of the median measured velocity). This suggests that pressure recordings at other locations can be used to estimate the corresponding wave-related velocity moments.

As only pressure is measured at site S2, the mean flow velocity at this location is estimated using the concept of continuity. Here, it is assumed that the cross-shore flux of water at S1 due to the rising and falling of the tide is equal to the volume of water flowing over the chenier crest when it is submerged. This means that $\overline{u}$ can be estimated by scaling the current velocity measured by the ADV to the ratio of the water depth at the location of the ADV over the water depth on top of the chenier.

For the calculation of both the pressure- and continuity-derived velocity moments, a minimum water depth of 10 cm has been applied to avoid erroneous velocity estimates due to inherent measurement uncertainty of the bed profile at the chenier top.

3. Results

3.1. Observations

3.1.1. Bathymetry

Figure 4 shows the profiles measured between 28 November 2018 and 4 December 2018. Mean Sea Level corresponds to $z = 0$, the origin of the x-axis is situated at the WaveDroid offshore (S0), and the coastline is around $x = 5800$. The landward end of the measured transect represents the edge of the sand body, which is separated from the coastline by a mudflat of 200 m wide (see Figure 3). An estimate of the bathymetry of the mudflat, based on point measurements using a rod and handheld GPS, is shown by the dashed line in Figure 4. The three frames on which instruments were mounted are also indicated, S1 seaward of the chenier, at a submerged bar (around $x = 5425$) with an ADV and a wave logger, S2 just seaward of the chenier crest (around $x = 5520$), with a wave logger and S3 landward of the chenier (around $x = 5620$) with a wave logger.

Despite relatively mild hydrodynamic conditions, the chenier migrated surprisingly fast in the landward direction. The emerged part of the chenier ($5550 < x < 5590$) migrated approximately 20 m landward between 1 and 2 December 2018. However, the submerged part of the chenier remained relatively stable, notably the two submerged bars around $x = 5420$ and $x = 5450$. This quick migration took place during spring tide conditions, but also during relatively high wave conditions, as is elaborated in the following sections.

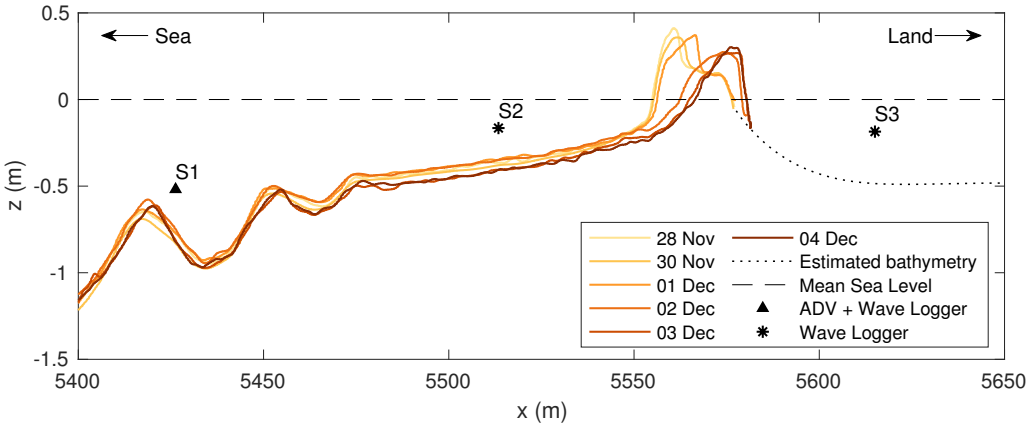

Figure 4. Profiles (see Figure 3d for location) measured daily with a Differential Global Positioning System (DGPS) between 28 November 2018 and 4 December 2018. The black dotted line gives an estimate of the bathymetry of the mudflat landward of the chenier. The two black asterisks indicate the location of two wave loggers, the black triangle of the frame with the Acoustic Doppler Velocimeter (ADV) and a wave logger. Mean Sea Level (black dashed line) corresponds to $z = 0$. The origin of the x-axis is the location of the WaveDroid offshore (S0, see Figure 1 for location), and the coastline is around $x = 5800$.

3.1.2. Hydrodynamics

Water levels were measured with pressure sensors at S1, S2 and S3. The mean spring tidal range is around 1 m (Figure 5a), so the tidal regime can be classified as micro-tidal [23]. Tidal analysis (using UTide [24]) provided tidal constituents revealing that the form factor is 1.72. Therefore, the tide can be classified as mixed, mainly diurnal characterized by two distinct spring-neap cycles overlapping two times per year [23,25]. Despite the diurnal dominance, the relatively large difference between O1 (0.08 m) and K1 (0.22 m) leads to a limited spring-neap variation of the diurnals, whereas the small difference between S2 (0.08 m) and M2 (0.10 m) leads to a pronounced spring-neap variation of the semi-diurnals.

The measured wave height was generally low (Figure 5b). The highest waves typically occur in the afternoon, when the prevailing weak south-east monsoon wind is overruled by a stronger onshore sea breeze (the purple dots in Figure 5d show the wind direction measured at a monitoring station in Semarang [26]). The sea breeze generates higher, longer and onshore directed waves. One exception to this daily trend can be observed on 2 December 2018, a period when higher, onshore waves, were observed during the early hours.

Figure 5e gives the cross-shore velocity, where positive is onshore directed, while Figure 5f shows the alongshore velocity, positive in north-eastern direction, away from Semarang. The blue line gives the instantaneous signal, whereas the orange line represents a moving average with a window of 30 min, representing the mean current.

3.2. Analysis

The observed cross-shore migration of the chenier is relatively fast and varying over time. The top of the chenier migrates landward with a maximum speed of 8 m/day. In order to explain the rapid onshore migration (see Figure 4), we decompose the observed hydrodynamic data into velocity moments (see Section 2).

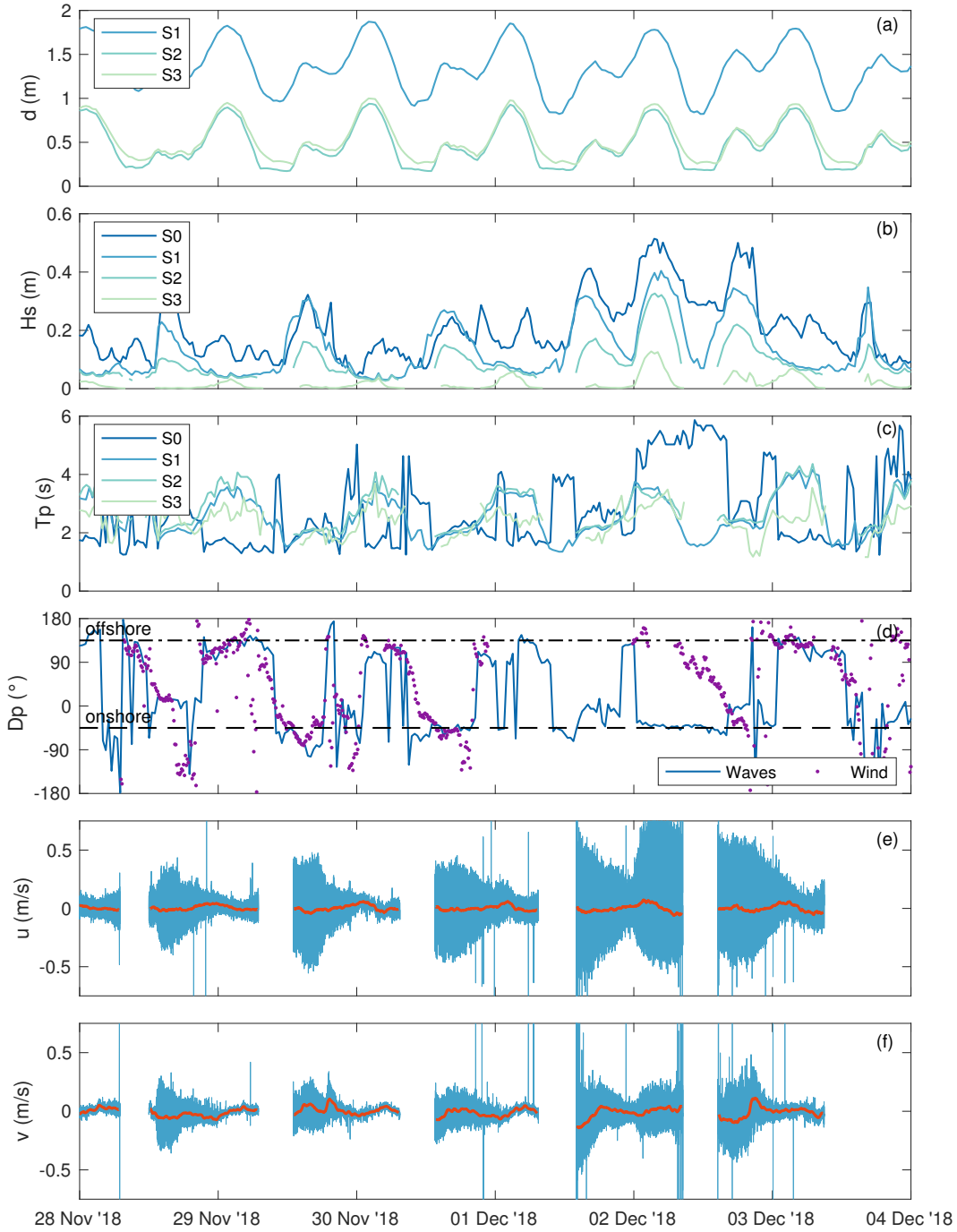

Figure 5. Hydrodynamic conditions between 28 November and 4 December 2018: (**a**) water depth, (**b**) significant wave height, (**c**) peak wave period, (**d**) peak wave and wind direction (wrt north), (**e**) cross-shore velocity (positive in onshore direction) and (**f**) longshore velocity (positive in north-eastern direction, away from Semarang). The locations of the sensors are indicated in Figure 1 (S0, offshore station) and Figure 4 (S1–S3). The wave direction in (**d**) is measured by the WaveDroid at S0 and the wind direction is retrieved from a monitoring station in Semarang [26]. The velocities (**e**–**f**) are measured with an ADV at S1.

The cross-shore displacements of both the chenier crest (orange) and the submerged bar (blue) are shown in Figure 6a. During the first 2–3 days, the profile is fairly stable. After 1 December, the chenier crest migrates landward rapidly (around 5 meter per day). The submerged bar is less dynamic, only on 2 and 3 December, a small landward displacement is observed. The water level at both locations is

shown in Figure 6b. The dashed black line represents the height of the chenier crest, so when the water level exceeds this dashed line, the chenier is fully submerged (the periods when the chenier is fully submerged are shaded in gray in Figure 6b–f). Note that the submergence period depends on the tidal range, but also on the height of the chenier, which decreases over time (see also Figure 4).

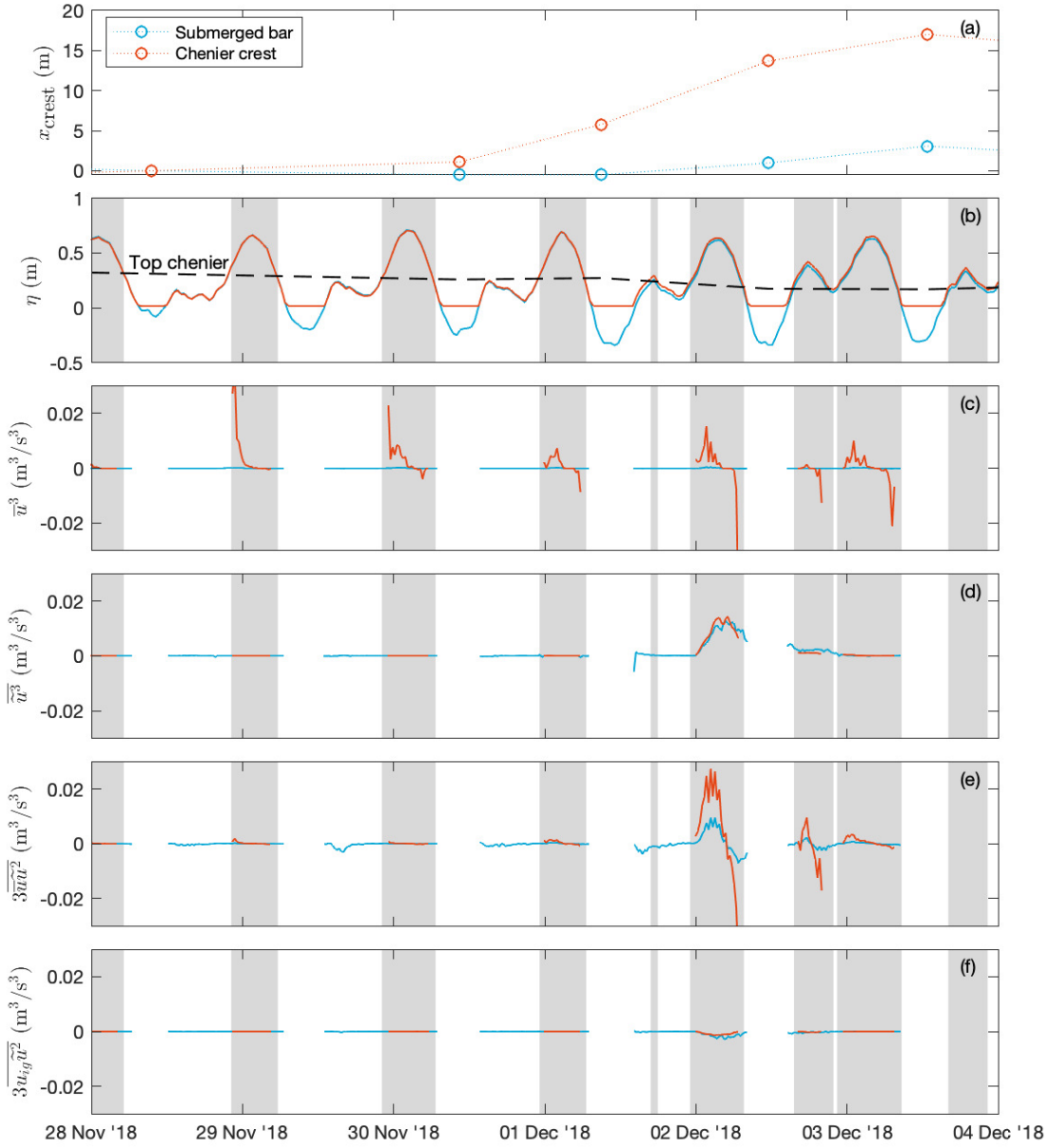

Figure 6. Time series at the submerged bar (blue) and chenier crest (orange) of (**a**) the cross-shore coordinate of the bar/chenier crest; (**b**) water level; (**c**) $\overline{u}^3$, mean current; (**d**) $\widetilde{\overline{u}^3}$, short waves; (**e**) $3\widetilde{\overline{u}}\widetilde{\overline{u^2}}$, stirring; (**f**) $3\overline{u_{ig}}\widetilde{\overline{u^2}}$, infragravity waves.

Figure 6c–f shows the velocity moments at two locations, in blue at the submerged bar, based on the ADV measurements, and in orange on top of the chenier, estimations based on pressure recordings and continuity (see Section 2, Appendix A and de Wit et al. [22] for a detailed explanation of the followed approach). The cumulative velocity moments, which are a good proxy for the net sediment transport, are given in Figure 7. The bar is always submerged during these 6 days, so the cumulative velocity moment is calculated over a continuous period. The chenier is only submerged during parts

of the 6 days. The cumulative velocity moments on top of the chenier are therefore only calculated for the periods when the chenier was completely submerged.

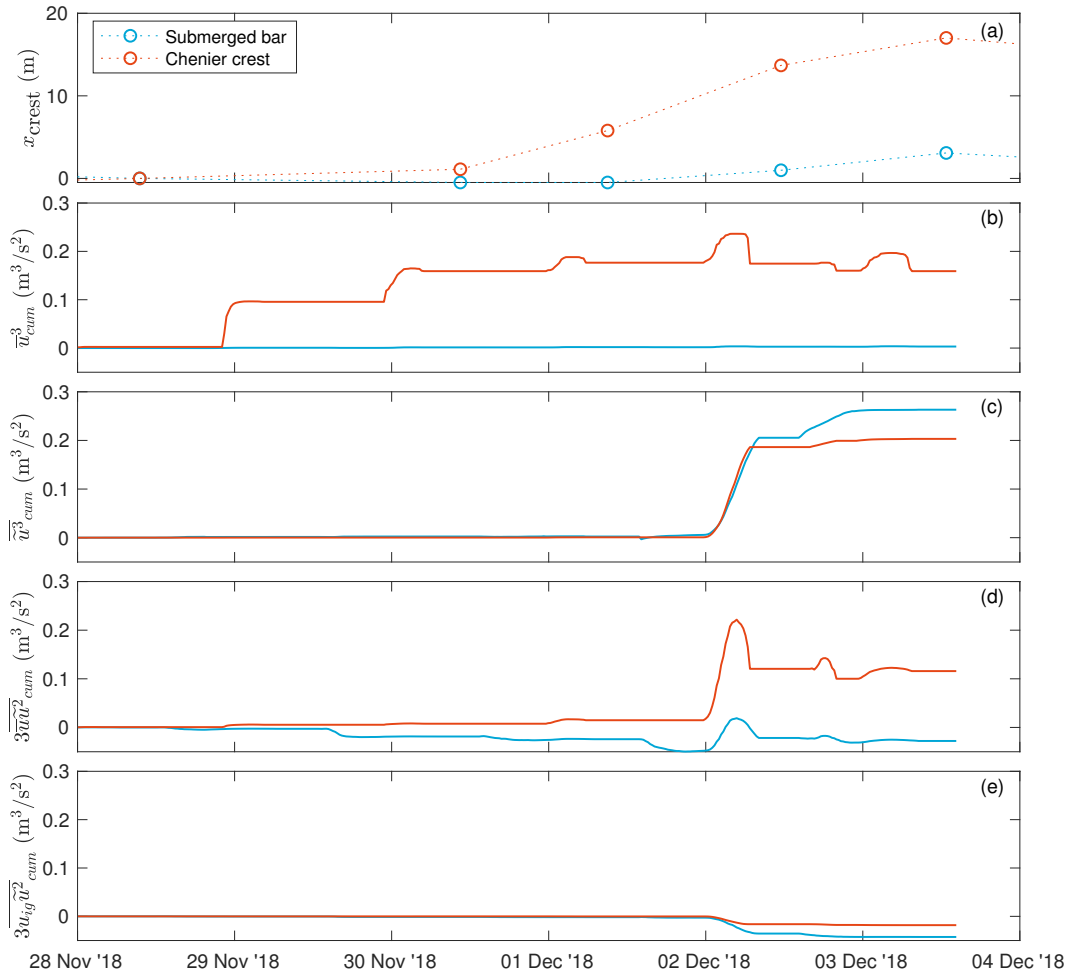

Figure 7. Cumulative velocity moments at the submerged bar (blue) and chenier crest (orange). (**a**) the cross-shore coordinate of the bar/chenier crest; (**b**) $\overline{u}^3_{cum}$, mean current; (**c**) $\overline{\widetilde{u}^3}_{cum}$, short waves; (**d**) $3\overline{\widetilde{u}\widetilde{u}^2}_{cum}$, stirring; (**e**) $3\overline{u_{ig}\widetilde{u}^2}_{cum}$, infragravity waves.

3.2.1. Sediment Transport by Mean Current

Figure 6c gives $\overline{u}^3$, representing the sediment transport driven by the mean current (mainly tidal, but also including wind and wave-driven components). At the location of the submerged bar (blue line), $\overline{u}^3$ is insignificant. However, on top of the chenier, $\overline{u}^3$ becomes significant, especially when the water depth is small at the start and end of the submergence periods (indicated by the gray shaded areas). On 2 December, $\overline{u}^3$ is higher than on other days around the same time, probably due to an additional wave set-up.

The cumulative velocity moment (a proxy for the net sediment transport) due to the mean current is negligible at the location of the submerged bar, as the instantaneous velocity moments are small as well. The crest of the chenier experiences a net landward transport at each tidal cycle for the first couple of days. The last two days, however, the landward directed transport during the first hours of high tide is balanced by an offshore directed transport during the last hour of submergence. This flow reversal can be explained by the spatial variability of the chenier: when the chenier crest is high relative to the water level, the ebb tide mainly flows around the chenier (through an opening south-west of the chenier, see Figure 3). However, as the height of the chenier crest decreases (both in absolute terms because of morphological changes, but also relatively because of higher high water levels), part of the ebb tide flows back over the chenier, thereby transporting sediment offshore.

3.2.2. Sediment Transport by Short Waves

The first four days, the waves are low and therefore $\overline{\widetilde{u}^3}$ is zero (see Figure 6d). On 2 December, the waves are higher, resulting in positive velocity moments at both locations. While the wave height is lower on top of the chenier (see Figure 5), the water depth is lower as well, so the orbital velocities near the bed remain relatively high. During the afternoon of 2 December, the sea breeze-induced waves occur around mean sea level (MSL) and therefore the chenier is not fully submerged. By the time the chenier becomes fully submerged, the wave height has decreased, leading to smaller velocity moments.

The cumulative velocity moments (see Figure 7c) remain close to zero over the first four days. In the early hours of 2 December at high tide, a positive net sediment transport is generated at both observation locations. In the afternoon, during conditions with wind waves generated by the sea breeze, an additional positive sediment transport is generated at the location of the submerged bar. On top of the chenier, this transport starts later because the chenier is not submerged yet. However, as the wave height has decreased during the period of high tide, the wave-generated transport is much lower.

Short waves (when present) generally generate net positive sediment transport, due to relatively large skewness and negative asymmetry (not shown). During the week of field observations, the sea breeze coincided with tidal elevations around MSL, when the chenier crest was not submerged. Therefore, wave skewness plays a more important role in the sediment transport over the submerged bar, than over the top of the chenier.

3.2.3. Sediment Transport by Stirring

Stirring, shown in Figure 6e, is the combined effect of the mean current and short waves; the waves stir up the sediment from the bed and the mean current transports it. The transport direction is therefore identical to the transport by the mean flow (see Figure 6c). At the location of the submerged bar, $3\overline{\widetilde{u}\widetilde{u}^2}$ is mostly negligible up to 2 December, with a small but persistent negative value around MSL. This is consistent with the presence of a return flow to compensate for the wave-induced mass flux [27] at times of the sea breeze. This wave-related mean flow effect is absent on top of the submerged chenier as the waves are very small during high tide (see Figure 5a,b). On 2 December, $3\overline{\widetilde{u}\widetilde{u}^2}$ is large and landward directed during a time when the chenier is fully submerged, the tide is rising and the wave height is (relatively) high. The values are significantly larger at the chenier crest than at the submerged bar, which is due to a larger mean current due to the smaller water depth, while the orbital velocities near the bed are comparable at both locations. The velocity moment changes sign during the last hours of submergence of the chenier crest, because of the offshore-directed mean flow during ebbing consistent with the mean velocity moments discussed earlier.

The cumulative of $3\overline{\widetilde{u}\widetilde{u}^2}$ (see Figure 7d), representing the net sediment transport due to stirring, reveals a small negative transport over the first four days at the submerged bar. The last two days, when the waves are higher, the net transport is more or less zero, because the transport rates during ebbing and flooding are nearly equal but opposite. On the chenier top, the cumulative effect is zero during the first days, because the waves are small at the time of submergence. On 2 December, the high waves combined with an onshore mean current generate a strong, positive sediment transport, which is only partially compensated during falling tide. This is different from the mean-flow moment and can be explained by the fact that although the mean flow reversal is symmetric, the waves are larger during the rising tide than during the falling tide (see Figure 5a,b). On December 3rd, the waves are more or less constant in height but smaller and the net transport is zero, consistent with the mean flow transport.

3.2.4. Sediment Transport by Infragravity Waves

The infragravity waves are negligible during the first four days, therefore the velocity moments are zero as well (see Figure 6f). On the morning of 2 December, $3\overline{u_{ig}\widetilde{u}^2}$ is negative at both locations.

This is the result of a negative correlation between the short wave envelope and the infragravity waves [20] consistent with the presence of bound infragravity waves.

The cumulative velocity moments (see Figure 7e) remain close to zero over the first four days. On the morning of 2 December, sediment transport is seaward at both locations. The cumulative transport over the submerged bar is two times higher than the transport over the chenier crest, but both contributions are relatively small, compared to the other transport mechanisms discussed earlier.

3.2.5. Combined Sediment Transport

Figure 8 shows the cumulative velocity moments of all processes combined on the right y-axis, and the displacement of the bed in cross-shore direction on the left y-axis. Note that there is no difference in scaling between the two locations, so the net transport on top of the chenier is around twice the net transport at the submerged bar, whereas the displacement of the chenier crest is around three times the displacement of the submerged bar. With this constant scaling the cumulative velocity moments show a close correspondence to the cross-shore displacement of both the bar crest and the chenier top.

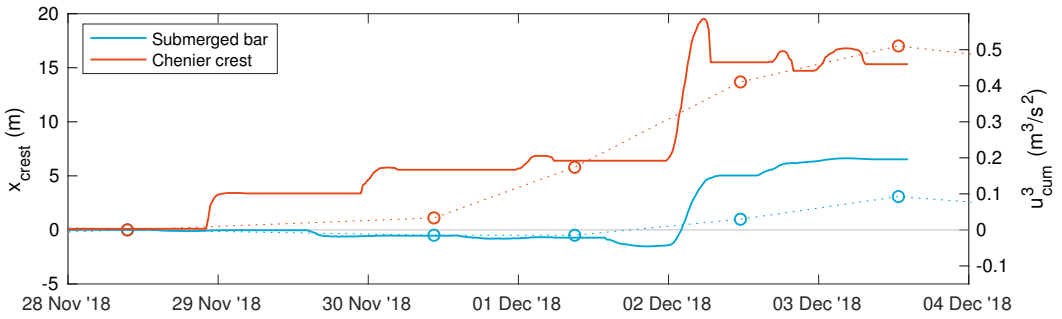

Figure 8. Crest displacements x_{crest} (left y-axis, circles connected by dotted lines) versus cumulative velocity moments $\overline{u^3}_{cum}$ (right y-axis, solid lines) at the submerged bar (blue) and chenier crest (orange).

During relatively calm periods, the mean current transport is too small to influence the bottom profile at the submerged bar, but is the dominant contribution in sediment transport over the chenier when it is submerged. With a relatively high crest elevation this leads to a net onshore transport as the ebb currents are diverted by larger-scale topographic effects flowing around the chenier (see Figure 3). When the chenier becomes relatively lower, the ebb currents also partially flow over the chenier crest, resulting in equal ebb and flood transports and thereby negligible net sediment transport.

In the presence of relatively high waves when the chenier is emerged, a relatively small offshore-directed sediment transport occurs at the submerged bar, caused by stirring. When relatively high waves occur during a time when the chenier is submerged, relatively large landward-directed sediment transports occur both at the submerged bar and on top of the chenier. During these periods, skewness and stirring are the dominant mechanisms. Where skewness only generates landward transport, the net transport by stirring is determined by the timing of the waves and the (reversing) mean flow. Infragravity waves do not contribute significantly to the sediment transport at this location.

4. Discussion

4.1. Importance of Local Sea Breeze

Our field observations were collected during the south-east monsoon season, a period during which the wind is persistently blowing from land to sea. Due to the resulting limited fetch length, the waves generated by the offshore monsoon wind are very short and only marginally stir up sediment. However, during this season a persistent sea breeze develops in the afternoon. The wind waves generated by this onshore wind are typically much larger than the S.E. monsoon-generated waves.

The first four days of the measurement period are a good representation of the typical conditions during the S.E. monsoon season. Despite the sea breeze generating higher waves, this does not lead to significant sediment transport. Most sediment transport takes place on 2 December, during a local wind event unrelated to the sea breeze. These waves contributed strongly to net displacement of the chenier, partly because the wave height is slightly larger than those resulting from the sea breeze, but mainly due to the phase shift between high waves and high tide. The 2 December event generated high waves around high water, whereas the sea breeze resulted in high waves during the afternoon, when water levels are low (and therefore the chenier crest was not submerged).

While the timing of the sea breeze is the same throughout the entire S.E. monsoon season (the afternoon), the timing of the diurnal high tide shifts through the day. Figure 9 shows the time of the highest water level per day for the year 2018. During the months of June–September, the highest water level of the day occurs in the afternoon, coinciding with the sea breeze. This will likely lead to higher sediment transport and therefore to even more dynamic cheniers. However, most of the high tides are relatively low, which will reduce the sediment transport, as the chenier may not always be submerged at high tide, reducing the dynamics of the cheniers.

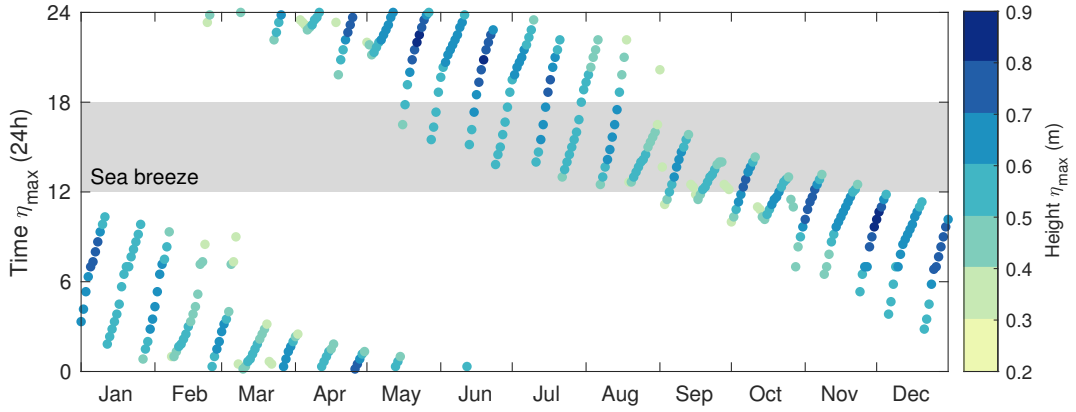

Figure 9. Time of the highest water level of the day for the year 2018 (reconstructed using UTide [24]). The colour scale represents the height of the highest water level of the day. The shaded area indicates the period when the sea breeze occurs (between 12h00 and 18h00).

4.2. Analogue with Breaker Bars

The observed profiles reveal the presence of two submerged sand bars (see Figure 4) resembling breaker bars commonly observed at sandy coastlines. The dynamics of these breaker bars have been studied extensively (in contrast to the short-term dynamics of chenier bars), and therefore we evaluate to what extent the known dynamics of breaker bars also represent the dynamics of chenier bars.

Ruessink et al. [28] compared a large number of breaker bars, and concluded that the cross-shore bar length L_{bar} is exponentially related to the water depth above the bar d_{bar} as in:

$$L_{bar} = 100 \exp(0.27 \times d_{bar}) \quad (3)$$

which yields a length of $O(100)$ m using the bar depth near S1. This is slightly longer than observed, however their data set considered bar systems with larger bar depths, resulting in a less accurate description of breaker bar length at smaller depths. This suggests that these bars are indeed breaker bars that have been formed during storm conditions. Breaker bars are known to propagate onshore during mild non-breaking conditions due to wave skewness, asymmetry and boundary layer streaming effects (e.g., [29–32]). This is consistent with the current observations where the onshore displacement of the bar crest coincides with the presence of waves with significant skewness (see Figure 6). These higher waves coincide with high tide (see Figure 5), resulting in a wave height over water depth ratio of less than 0.3, consistent with non-breaking waves over the bar crest (e.g., [33]). It is expected that the breaker bars move offshore during storm conditions, consistent with the observed bar behaviour

along open sandy coasts (e.g., [34]), but this cannot be supported by the current observations as only non-storm conditions were observed.

The cross-shore migration rate for the chenier top is much faster than for the submerged bars resulting in a much larger cross-shore displacement (see Figure 6a). This rapid onshore displacement coincides with the submergence of the chenier crest and as such is more in line with swash bars that have been observed to propagate rapidly onshore during mild submergence ([35,36]). This rapid displacement is attributed to the fact that waves propagate over the inter-tidal bar where the wave-related mass transport subsequently is seaward through lateral runnels (e.g., [36]). Here, the presence of the bay behind the chenier acts like a runnel, preventing the wave-related mass flux to create a return current, thus enhancing the onshore mean flow over the chenier top. In that case both the stirring and wave non-linearity become very effective in transporting sediment onshore, resulting in a rapid onshore motion.

Note that the cross-shore displacement of both breaker bars and chenier crest are the result of cross-shore changes in the sediment transport. The analyses presented here are based on measurements close to the crest of the breaker bars and the chenier top where the locally maximum sediment transport is expected to occur. As such they are expected to be a good indicator of both the propagation direction and migration rate of these features (e.g., [29,30]).

4.3. Influence of Hydrodynamic Conditions

This paper presents a semi-quantitative approach using an energetics-based approach using velocity moments to estimate the sediment transport [18,19]. However, with the field data alone, it is not possible to completely quantify the sediment transport, nor is it possible to estimate the sediment transport during other conditions. It was hypothesized that the phase shift between the sea breeze (always in the afternoon) and the period of high tide (regulated by the phase inclination of the O1 and K1 tidal constituents) will lead to more dynamic bar behaviour during monsoon conditions. Also, counterbalancing mechanisms (leading to an offshore migration of the submerged bars and the chenier crest) have not yet been quantified, although satellite images (Figure 3) reveal offshore migration during the monsoon season. Also, the analogue with breaker bars suggests storms provide conditions for seaward migration.

As a next step, the sediment transport mechanisms during other hydrodynamic conditions will be explored in more detail using a numerical model. Such an approach will reveal to what extent the onshore migration during calm conditions is indeed counterbalanced by offshore migration during storm conditions. The model will then be utilized to determine to what extent the phasing of the high water levels (gradually shifting throughout the year) relative to the sea breeze influences the dynamics of the chenier during the S.E. monsoon season. Finally, such a numerical approach would allow us to analyse the influence of the tidal basin behind the chenier on chenier dynamics, by exploring various spring tide and storm set-up scenarios.

5. Conclusions

Cheniers can play an important role in stabilising a coastline. This paper presents and analyses a week of field observations of a chenier along the coast of Demak, Indonesia. Under relatively calm hydrodynamic conditions, the chenier migrated landwards relatively fast (the chenier top moved at speeds between 0.5 and 8 m/day). Using velocity moments as a proxy for the sediment transport, the role of the tide and waves on the cross-shore chenier dynamics was investigated by means of a decomposition of the velocity in mean current, short wave and long wave contributions.

During calm conditions (representative for the S.E. monsoon season, Hs smaller than 0.5 m at deep water), the tide generates substantial sediment transport in very shallow water only. When the chenier is relatively high (height crest compared to high tide), this transport is landward-directed, because the ebb currents prefer to flow around instead of over the chenier.

Waves transport sediment directly through skewness and indirectly through stirring. In the S.E. monsoon season, most of the significant waves are generated by a sea breeze in the afternoon. However, during the field measurements, the chenier was not submerged in the afternoon (high tide was during the night). This resulted in a small net offshore sediment transport at the submerged bars and negligible transport at the chenier crest. On 2 December, a local wind event unrelated to the sea breeze took place during high tide. This caused significant (landward-directed) sediment transport due to waves, both through skewness and stirring.

The field observations show that both tide and waves transport sediment, thus driving the cross-shore chenier dynamics. Whereas the magnitude of both play a role, it is mainly the timing of the higher waves and the higher water levels that is crucial for the cross-shore chenier dynamics. When the high waves occur during high tide, cheniers show behaviour similar to swash bars. Since the field observations took place during the calmer, S.E. monsoon season, they do not reveal mechanisms responsible for the cross-shore chenier dynamics during the N.W. monsoon season, including storm conditions. These conditions will be explored in more detail using a numerical model as part of future work.

Author Contributions: S.A.J.T.: collection, post-processing and analysis of field data; writing. D.S.v.M.: conceptualization, writing and review; A.J.H.M.R.: analysis wave data, conceptualization, writing and review. All authors have read and agreed to the published version of the manuscript.

Funding: This work is part of the BioManCO project with project number 14753, which is (partly) financed by NWO Domain Applied and Engineering Sciences, and co-financed by Boskalis Dredging and Marine Experts, Van Oord Dredging and Marine Contractors bv, Deltares, Witteveen+Bos and Wetlands International.

Acknowledgments: The BioManCO project, initiated and coordinated by Han Winterwerp, is a collaboration between Delft University of Technology, NIOZ and Universitas Diponegoro (UNDIP) and makes use of the framework set up by Building with Nature Indonesia, a programme by Ecoshape, Wetlands International, the Indonesian Ministry of Marine Affairs and Fisheries (MMAF), the Indonesian Ministry of Public Works and Housing (PU) and other partners. The field work was organised in collaboration with Alejandra Gijón Mancheño and Celine van Bijsterveldt and co-supervised by Muhammad Helmi. In the field we received assistance from staff and students of UNDIP. We also would like to thank the families of Pak Slamet and Pak Matsaeri for hosting us in Timbulsloko.

Conflicts of Interest: The authors declare no conflict of interest.

Data Availability Statement: The measurement data is available in the repository of 4TU.ResearchData, with the doi: https://doi.org/10.4121/13177388.

Abbreviations

The following abbreviations are used in this manuscript:

ADV	Acoustic Doppler Velocimeter
DGPS	Differential Global Positioning System
FFT	Fast Fourier Transform
MSL	Mean Sea Level
N.W.	north-west
RMSE	Root Mean Square Error
S.E.	south-east
S#	frame with instruments, frame number # increasing from offshore to nearshore

Appendix A. Estimate Velocity from Pressure Signal

To obtain pressure-derived velocities use is made of linear wave theory following the approach of de Wit et al., 2019 [22]. The wave-related pressure for a monochromatic wave with radial frequency ω is given by:

$$p_{wave}(z,t) = \rho g a \frac{\cosh(k(h+z))}{\cosh(kh)} \cos(\omega t + \phi_p) \quad \text{(A1)}$$

where z is the vertical elevation (defined positive upward from the mean water level), ρ the water density, g the gravitational constant, a the wave amplitude, h the local water depth, ϕ_p is a phase shift and the wave number k is obtained through the dispersion relation $\omega = \sqrt{gk\tanh(kh)}$. The corresponding expression for the horizontal orbital velocity is given by:

$$u_{wave}(z,t) = \omega a \frac{\cosh(k(h+z))}{\sinh(kh)} \cos(\omega t + \phi_u) \tag{A2}$$

with ϕ_u a velocity phase shift. In case of progressive waves, the wave related pressure and velocity are in phase, hence $\phi_p = \phi_u$, and these two expressions can be combined to express the wave orbital velocity as function of the pressure:

$$u_{wave}(z,t) = p_{wave}(z,t)\frac{\omega}{\rho g}\frac{\cosh(kh)}{\sinh(kh)} = T(z,\omega)p_{wave}(z,t) \tag{A3}$$

with T as the frequency-dependent transfer function.

Next the ADV-measured half-hour pressure record at location S1 is transformed with a Fast Fourier Transform (FFT) and multiplied with the frequency-dependent transfer function $T(\omega)$. Taking the inverse FFT then yields the pressure-derived velocity record. Comparing the cumulative velocity moments at S1 obtained with the measured horizontal velocity and the pressure derived velocities shows a good match with root mean square errors in the order of 10%. Figure A1 shows the cumulative velocity moments calculated using the measured velocities (blue line) and the pressure-derived velocities (yellow line). Both lines show the same behaviour, but the magnitude of the pressure-derive velocity moments is slightly underestimated. Since this approach can only be used to estimate the wave orbital velocity, the measured mean velocity at the ADV is used to calculate the stirring for both the measured and pressure-derived velocity moments.

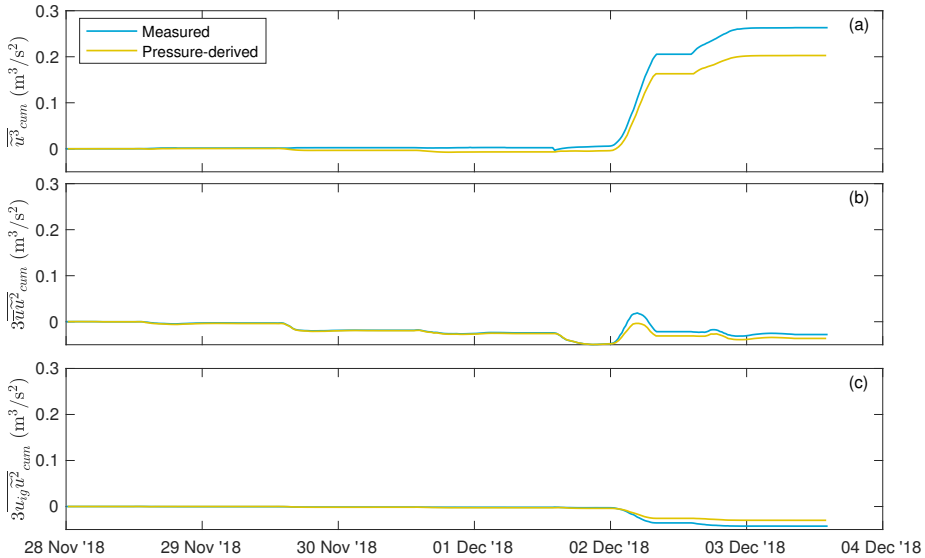

Figure A1. Cumulative velocity moments calculated using the measured velocities (blue) and the pressure-derived velocities (yellow). (**a**) $\overline{\tilde{u}^3}_{cum}$, short waves; (**b**) $3\overline{\tilde{u}\tilde{u}^2}_{cum}$, stirring; (**c**) $3\overline{u_{ig}\tilde{u}^2}_{cum}$, infragravity waves.

References

1. Otvos, E.G.; Price, W.A. Problems of chenier genesis and terminology—An overview. *Mar. Geol.* **1979**, *31*, 251–263. [CrossRef]
2. Augustinus, P.G.E.F. Cheniers and chenier plains: A general introduction. *Mar. Geol.* **1989**, *90*, 219–229, [CrossRef]

3. Anthony, E.J.; Brunier, G.; Gardel, A.; Hiwat, M. Chenier Morphodynamics on the Amazon-Influenced Coast of Suriname, South America: Implications for Beach Ecosystem Services. *Front. Earth Sci.* **2019**, *7*, 1–20, [CrossRef]
4. Nardin, W.; Fagherazzi, S. The Role of Waves, Shelf Slope, and Sediment Characteristics on the Development of Erosional Chenier Plains. *Geophys. Res. Lett.* **2018**, *45*, 8435–8444. [CrossRef]
5. Van Maren, D.S. Barrier formation on an actively prograding delta system: The Red River Delta, Vietnam. *Mar. Geol.* **2005**, *224*, 123–143. [CrossRef]
6. Russell, R.J.; Howe, H.V. Cheniers of Southwestern Louisiana. *Geogr. Rev.* **1935**, *25*, 449–461, [CrossRef]
7. Mcbride, R.A.; Taylor, M.J.; Byrnes, M.R. Coastal morphodynamics and Chenier-Plain evolution in southwestern Louisiana, USA: A geomorphic model. *Geomorphology* **2007**, *88*, 367–422. [CrossRef]
8. Cangzi, L.; Walker, H.J. Sedimentary Characteristics of Cheniers and the Formation of the Chenier Plains of East China. *J. Coast. Res.* **1989**, *5*, 353–368.
9. Anthony, E.J. Chenier plain development in northern Sierra Leone, West Africa. *Mar. Geol.* **1989**, *90*, 297–309. [CrossRef]
10. Anthony, E.J. Beach-ridge development and sediment supply: examples from West Africa. *Mar. Geol.* **1995**, *129*, 175–186. [CrossRef]
11. Van Bijsterveldt, C.E.J. Natural Mangrove Restoration: How Can it be Induced? Master's Thesis, Utrecht University, Utrecht, the Netherlands, 2015.
12. van Bijsterveldt, C.E.J. Can Cheniers Protect Mangroves Along Eroding Coastlines? in prep.
13. Lohmann, U.; Sausen, R.; Bengtsson, L.; Cubasch, U.; Perlwitz, J.; Roeckner, E. The Köppen climate classification as a diagnostic tool for general circulation models. *Clim. Res.* **1993**, *3*, 177–193. [CrossRef]
14. Putranto, T.T.; Rüde, T.R. Hydrogeological Model of an Urban City in a Coastal Area, Case study: Semarang, Indonesia. *Indones. J. Geosci.* **2016**, *3*, 17–27. [CrossRef]
15. Lang, C. Kaart van den Spoorweg van Samarang Naar de Vorstenlanden, 1869. Available online: http://hdl.handle.net/1887.1/item:811882 (accessed on 14 October 2020).
16. Marfai, M.A.; King, L. Monitoring land subsidence in Semarang, Indonesia. *Environ. Geol.* **2007**, *53*, 651–659. [CrossRef]
17. Google Earth 7.3.3. Satellite Images of Demak, Indonesia between 2015 and 2018. Available online: https://earth.google.com/web/ (accessed on 14 October 2020).
18. Bowen, A.J. Simple models of nearshore sedimentation: Beach profiles and longshore bars. *Coastline Can.* **1980**, 1–11. [CrossRef]
19. Bailard, J.A.; Inman, D.L. An Energetics Bedload Model for a Plane Sloping Beach: Local Transport. *J. Geophys. Res.* **1981**, *86*, 2035–2043. [CrossRef]
20. Roelvink, J.A.; Stive, M.J.F. Bar-Generating Flow Mechanisms on a Beach. *J. Geophys. Res.* **1989**, *94*, 4785–4800. [CrossRef]
21. Thornton, E.B.; Humiston, R.T.; Birkemeier, W. Bar/trough generation on a natural beach. *J. Geophys. Res.* **1996**, *101*, 12097–12110. [CrossRef]
22. De Wit, F.; Tissier, M.; Reniers, A.J.H.M. Characterizing Wave Shape Evolution on an Ebb-Tidal Shoal. *J. Mar. Sci. Eng.* **2019**, *7*, 367. [CrossRef]
23. Pugh, D.T. *Tides, Surges and Mean Sea-Level*, Reprinted with Corrections June 1996 ed.; John Wiley & Sons Ltd.: Wiltshire, UK, 1987; p. 472.
24. Codiga, D.L. *Unified Tidal Analysis and Prediction Using the UTide Matlab Functions*; Technical Report 01; Graduate School of Oceanography, University of Rhode Island: Narragansett, RI, USA, 2011; p. 59. [CrossRef]
25. Van Maren, D.S.; Gerritsen, H. Residual flow and tidal asymmetry in the Singapore Strait, with implications for resuspension and residual transport of sediment. *J. Geophys. Res.* **2012**, *117*, 1–18. [CrossRef]
26. Badan Meteorologi Klimatologi dan Geofisika. Automatic Weather Station Maritim Semarang. 2020. Available online: http://202.90.199.132/aws-new/monitoring/3000000014 (accessed on 14 January 2019).
27. Dyhr-Nielsen, M.; Sorensen, T. Some sand transport phenomena on coasts with bars. *Coast. Eng.* **1970**, 855–865. [CrossRef]
28. Ruessink, B.G.; Wijnberg, K.M.; Holman, R.A.; Kuriyama, Y.; van Enckevort, I.M.J. Intersite comparison of interannual nearshore bar behavior. *J. Geophys. Res.* **2003**, *108*. [CrossRef]
29. Gallagher, E.L.; Elgar, S.; Guza, R.T. Observations of sand bar evolution on a natural beach. *J. Geophys. Res.* **1998**, *103*, 3203–3215. [CrossRef]

30. Hoefel, F.; Elgar, S. Wave-induced sediment transport and onshore sandbar migration. *Science* **2003**, *299*, 1885–1887. [CrossRef]
31. Henderson, S.M.; Allen, J.S.; Newberger, P.A. Nearshore sandbar migration predicted by an eddy-diffusive boundary layer model. *J. Geophys. Res.* **2004**, *109*. [CrossRef]
32. Ruessink, B.G.; Kuriyama, Y.; Reniers, A.J.H.M.; Roelvink, J.A.; Walstra, D.J.R. Modeling cross-shore sandbar behavior on the timescale of weeks. *J. Geophys. Res.* **2007**, *112*. [CrossRef]
33. Robertson, B.; Hall, K.; Zytner, R.; Nistor, I. Breaking waves: Review of characteristic relations. *Coast. Eng. J.* **2013**, *55*. [CrossRef]
34. Walstra, D.J.R.; Reniers, A.J.H.M.; Ranasinghe, R.; Roelvink, J.A.; Ruessink, B.G. On bar growth and decay during interannual net offshore migration. *Coast. Eng.* **2012**, *60*, 190–200. [CrossRef]
35. Cohn, N.; Ruggiero, P. The influence of seasonal to interannual nearshore profile variability on extreme water levels: Modeling wave runup on dissipative beaches. *Coast. Eng.* **2016**, *115*, 79–92. [CrossRef]
36. Vos, S.; Spaans, L.; Holman, R.; Mccall, R.; de Vries, S. Cross-Shore Intertidal Bar Behavior along the Dutch Coast: Laser Measurements and Conceptual Model. in prep.